Crystal field effects in the intermetallic $R\mathrm{Ni_3Ga_9}$ (R = Tb, Dy, Ho, and Er) compounds

L. S. Silva,[1] S. G. Mercena,[1] D. J. Garcia,[2] E. M. Bittar,[3] C. B. R. Jesus,[4] P. G. Pagliuso,[4] R. Lora-Serrano,[5] C. T. Meneses,[1] and J. G. S. Duque[1,4]

[1]*Programa de Pós-Graduação em Física, Campus Prof. José Aluísio de Campos, UFS, 49100-000 São Cristóvão, SE, Brazil*

[2]*Consejo Nacional de Investigaciones Científicas y Técnicas (CONICET) and Centro Atómico Bariloche, RA-8400 S.C. de Bariloche, Río Negro, Argentina*

[3]*Centro Brasileiro de Pesquisas Físicas, Rua Dr. Xavier Sigaud 150, 22290-180 Rio de Janeiro, RJ, Brazil*

[4]*Instituto de Física "Gleb Wataghin", UNICAMP, 13083-970 Campinas-São Paulo, Brazil*

[5]*Instituto de Física, Universidade Federal de Uberlândia, 38408-100 Uberlândia, MG, Brazil*

(Received 19 September 2016; revised manuscript received 5 January 2017; published 19 April 2017)

In this paper, we report temperature-dependent magnetic susceptibility, electrical resistivity, and heat-capacity experiments in the family of intermetallic compounds $R\mathrm{Ni_3Ga_9}$ (R = Tb, Dy, Ho, and Er). Single-crystalline samples were grown using Ga self-flux method. These materials crystallize in a trigonal $\mathrm{ErNi_3Al_9}$-type structure with space group $R32$. They all order antiferromagnetically with $T_N < 20$ K. The anisotropic magnetic susceptibility presents large values of the ratio $\chi_{\mathrm{easy}}/\chi_{\mathrm{hard}}$ indicating strong crystalline electric-field (CEF) effects. The evolution of the crystal-field scheme for each R was analyzed in detail by using a spin model including anisotropic nearest-neighbor Ruderman-Kittel-Kasuya-Yosida interaction and the trigonal CEF Hamiltonian. Our analysis allows one to understand the distinct direction of the ordered moments along the series—the Tb-, Dy-, and Ho-based compounds have the ordered magnetic moments in the easy ab plane and the Er sample magnetization easy axis is along the $\hat{c}$ direction.

DOI: 10.1103/PhysRevB.95.134434

I. INTRODUCTION

In 4f-electron systems with strong electronic correlations, the number of exuberant physical phenomena is remarkably wide. Quantum criticality, heavy fermion behavior, magnetic transitions, valence fluctuation, unconventional superconductivity, and non-Fermi-liquid behavior are examples of the rich variety of effects that can be observed in these materials depending on the hybridization between the 4f and conduction electrons (see Ref. [1] and references therein). The Ce- and Yb-based compounds are central pieces of these studies because their electronic configurations can be easily tuned by doping, external pressure, temperature, or applied magnetic fields. In fact, these parameters can frequently tune the competition between the Kondo effect and Ruderman-Kittel-Kasuya-Yosida (RKKY) interaction, which are originated from the exchange interaction between the 4f and conduction electrons. On the other hand, the magnetic properties of non-(Ce,Yb) analogs are usually of local-moment character and mainly depend on the interplay between crystalline electric-field (CEF) effects and exchange magnetic interaction. Thus, the study of structurally related compounds is a fertile ground to explore how the evolution of dimensionality and/or anisotropy effects along the series can affect the ground state of their members without dealing with a more complex set of interactions competing at the same energy scale.

Recently, single crystals of Yb-based Kondo lattice compounds $\mathrm{YbNi_3}X_9$ (X = Al, Ga) were successfully synthesized [2,3]. $\mathrm{YbNi_3Al_9}$ is an antiferromagnetic (AFM) heavy fermion system with $T_N = 3.4$ K. The magnetic susceptibility of $\mathrm{YbNi_3Ga_9}$, on the other hand, shows a broad maximum at about 200 K and the typical valence fluctuation behavior with Pauli paramagnetic ground states. The strong valence fluctuation agrees with the study of the electronic structure using photoemission spectroscopy [4]. The substitutional study on $\mathrm{YbNi_3(Ga_{1-x}Al_x)_9}$ revealed that the Kondo temperature T_K of $\mathrm{YbNi_3}X_9$ is reduced from 600 to 550 K with Al substitution of only $x = 0.1$ [3]. Furthermore, Matsubayashi *et al.* observed an unconventional quantum critical behavior in the $\mathrm{YbNi_3Ga_9}$ phase diagram as a function of pressure, magnetic field, and temperature [5]. Additionally, they have identified a Yb valence crossover at the vicinity of the critical pressure P_c of the pressure-induced AFM transition and a first-order metamagnetic transition at $H = 6.9$ kOe and $T = 0.4$ K possibly due to the valence instability.

The series $R\mathrm{Ni_3Al_9}$ which are isostructural analogues of the $\mathrm{YbNi_3Al_9}$ compound have been studied for R = Er, Gd, Y, and Dy [6,7] and R = Gd-Lu [8]. For R = Tb to Ho and Yb, the easy axis of magnetization is in the ab plane, while for R = Er and Tm it is along the $c$axis. Metamagnetic transitions were observed for R = Er, Tm, and Yb. It has been suggested that crystal-field effects may be responsible for some characteristic features observed in the specific-heat and magnetic susceptibility data.

Here, we report on the magnetic properties of a Ga-based analogs series of ternary rare-earth transition metals $R\mathrm{Ni_3Ga_9}$ (R = Tb, Dy, Ho, and Er), which have been grown as single-crystalline samples by the Ga self-flux method [9,10]. All compounds order antiferromagnetically with $T_N < 20$ K. The magnetic susceptibility presents large values of the ratio $\chi_{\mathrm{easy}}/\chi_{\mathrm{hard}}$, indicating strong CEF effects. We have followed the CEF evolution with R using a spin model including an anisotropic first-neighbor RKKY interaction and the trigonal CEF Hamiltonian [11,12]. Our results indicate that the tetragonal B_0^2 parameter is positive for $\mathrm{TbNi_3Ga_9}$, $\mathrm{DyNi_3Ga_9}$, and $\mathrm{HoNi_3Ga_9}$, which have an easy plane (ab) of magnetization, while it is negative for $\mathrm{ErNi_3Ga_9}$ with easy magnetization axis along the $\hat{c}$ direction. The presence of anisotropic metamagnetic transitions for $\mathrm{DyNi_3Ga_9}$, $\mathrm{HoNi_3Ga_9}$, and $\mathrm{ErNi_3Ga_9}$ at

$T = 2$ K has been observed. The inverse susceptibility data can be fitted to a Curie-Weiss (CW) law for $T > 100$ K for all compounds.

The paper is organized as follows. In Sec. II, we present the details of the experimental methods used for the measurements. Section III presents and discusses the data collected. Details of the spin model simulation to account for the CEF effects as a function of R will be also discussed. Finally, we present our conclusions.

II. EXPERIMENTS DETAILS

A. Sample preparation

Single crystals of $R\mathrm{Ni_3Ga_9}$ (R = Tb, Dy, Ho, and Er) were grown by Ga self-flux method. Starting elements with purities of 99.9% in a molar ratio of 1(R):3(Ni):30(Ga) were placed into an alumina crucible and sealed under vacuum in a quartz tube. The ampoules were then heated from room temperature to 1050 °C, kept at this temperature for 5 h, and slowly cooled down at 5 °C/h up to 650 °C, where the excess of Ga flux was decanted off from the plateletlike crystals by centrifugation.

B. Characterization techniques

The crystal symmetry and phase purity were studied by x-ray powder diffraction in the conventional $\theta - 2\theta$ Bragg-Brentano geometry using Cu K_α radiation. The Jana2006 software [13] was used for the Rietveld refinements of all the observed data. Specific-heat measurements were performed for samples ranged from 10 to 30 mg in a small-mass calorimeter system that employs a quasiadiabatic thermal relaxation technique (at $H = 0$). Magnetization measurements were collected in a commercial dc superconducting quantum interference device magnetometer. The susceptibility data were taken at $H = 1$ kOe in the temperature range between 2 and 300 K. For the M versus H curves, the applied field (H) was varied between 0 and 70 kOe at $T = 2$ K. In-plane electrical resistivity as a function of temperature was measured, at $H = 0$, using a low-frequency ac resistance bridge and four-contact configuration.

III. RESULTS AND DISCUSSION

Figure 1 shows the x-ray powder-diffraction patterns for the $R\mathrm{Ni_3Ga_9}$ samples taken at room temperature. The solid curves represent the calculated pattern from the model structure used in the Rietveld refinement to fit the experimental data. The solid line is the difference between experimental and calculated data. The vertical bars represent the Bragg peaks positions according to the model $\mathrm{ErNi_3Al_9}$-type structure [Crystallographic Open Database (COD: 96-210-0947)]. From these results the trigonal $\mathrm{ErNi_3Al_9}$-type structure, space group $R32$, can be confirmed for all the studied compounds. The goodness-of-fit parameters R_w, R_{wp}, and χ^2 for each refinement can be found in Table I. The inset of Fig. 1 shows the lattice-parameter evolution with increasing the atomic number (Z) of R from R = Tb to Er. As expected, a and c decrease with Z in agreement with the lanthanide contraction (see inset of Fig. 1 and Table I).

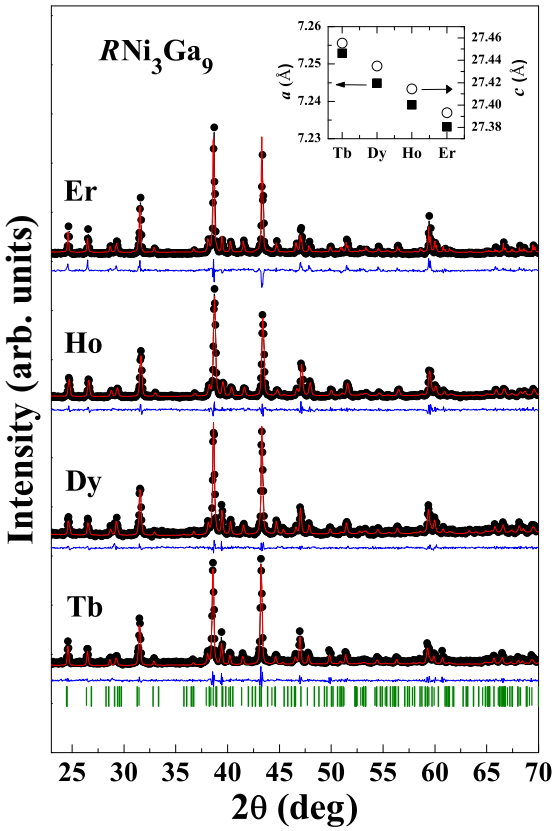

FIG. 1. Rietveld refinement of the x-ray powder-diffraction data (filled dot) for $R\mathrm{Ni_3Ga_9}$ at room temperature. The solid lines are the calculated and the difference between experimental and calculated patterns, respectively. The bars in the bottom panels represent the Bragg indexation according to the structural model, taken from the COD code 96-210-0947. The inset represents the evolution of the unit-cell parameters with R as extracted from the refinement. Error bars are smaller than the symbol sizes used.

The temperature dependence of the magnetic susceptibility measured for a magnetic field $H = 1$ kOe applied parallel $\chi_{//}$ (open symbols) and perpendicular $\chi_\perp$ (closed symbols) to the trigonal c axis is presented in Figs. 2(a)–2(d) for R = Tb, Dy, Ho, and Er, respectively. The inverse of the polycrystalline data (powder sample) is shown in the insets of Figs. 2(a) and 2(d). For Figs. 2(a) and 2(d), the maxima in the $\chi(T)$ data agree with the temperature at which the anomalies in the specific-heat and resistivity data take place (see below). These maxima usually occur at the vicinity of the onset of the long-range AFM order. The continuous curves in the χ versus T data were obtained from the spin model used to follow the evolution of the CEF perturbation with R (see below). It is evident that for $\mathrm{TbNi_3Ga_9}$ [Fig. 2(a)] there is a spontaneous easy axis of magnetization along the ab plane. This is clear because $\chi_\perp$ is much larger than $\chi_{//}$ near T_N and $\chi_\perp$ tends to rapidly decrease below T_N while $\chi_{//}$ remains nearly constant in this temperature range. For $\mathrm{ErNi_3Ga_9}$ [Fig. 2(d)], in contrast, there is an easy c-axis magnetization. From a linear fit to the inverse of χ_{poly} for $T > 100$ K using a CW law [solid lines in the insets of Figs. 2(a) and 2(d)], we extracted the CW temperature Θ_{CW} and the R^{3+} effective magnetic moment μ_{eff}

TABLE I. Experimental parameters extracted from Rietveld refinement (R_p, R_{wp}, χ^2, V, and c/a) and the magnetic susceptibility data (T_N, Θ_{CW}, μ_{eff}, and χ_{easy}/χ_{hard}).

	T_N (K)	Θ_{CW} (K)	μ_{eff} (μ_B)	χ_{easy}/χ_{hard}	R_p (%)	R_{wp} (%)	χ^2 (%)	V (Å^3)	c/a
$TbNi_3Ga_9$	17.1	−2.1	9.70	3.7	3.09	4.20	1.28	1444.27(2)	3.785
$DyNi_3Ga_9$	10.1	−2.7	10.59	2.97	3.08	4.10	1.20	1440.01(2)	3.786
$HoNi_3Ga_9$	4.7	−7.5	10.61	8.9	4.23	5.95	1.78	1436.64(3)	3.787
$ErNi_3Ga_9$	6.7	−6.2	9.53	14.7	4.42	6.18	1.76	1433.18(3)	3.787

(see Table I). The Dy- and Ho-based compounds [Figs. 2(b) and 2(c)] appear to be more complex at low T. In these two cases, the insets highlight the low-T region. For $DyNi_3Ga_9$, two maxima are observed for the $H//ab$ plane ($\chi_\perp$) below 10 K. When $H//c$ ($\chi_{//}$) more than one transition can be defined as well. $HoNi_3Ga_9$ presents a broad transition around 3.4 K for the $H//ab$ plane, while no anomalies can be observed for $H//c$. The higher ratios χ_{easy}/χ_{hard} (Table I) reflect the anisotropy of the magnetic susceptibility. These ratios are greater than 1 for all compounds, which is an indication of the presence of strong CEF effects.

The main panel of Fig. 3 shows the magnetic contribution to the specific heat divided by temperature (C_{mag}/T) in the temperature range $0 < T < 50$ K for $TbNi_3Ga_9$, $DyNi_3Ga_9$, $HoNi_3Ga_9$, and $ErNi_3Ga_9$ at zero applied field. The phonon contribution to specific-heat data for each magnetic compound was taken as the experimental data of the nonmagnetic $LuNi_3Ga_9$, which were subtracted from the total specific heat of each magnetic compound. The cusp in the specific-heat data, indicated by arrows, is associated with the onset of AFM order. The maxima observed in the magnetic susceptibility data (see Fig. 2) agree with the inflection point to the right side of the maxima in Fig. 3. Therefore, this temperature has been defined as T_N (see Table I). The shift of T_N to lower temperatures as the R ion size decreases is evident. For R = Er, a broad hump can be observed between 10 and 25 K. A similar behavior has been reported in Ref. [8] for $ErNi_3Al_9$ and was ascribed to CEF effects. For $DyNi_3Ga_9$ and $HoNi_3Ga_9$, the data do not drop to smaller values of C_{mag}/T at low temperature; instead, there is a tendency to increase in agreement with the behavior observed in their $\chi(T)$ data of Figs. 2(b) and 2(c). Additional magnetization and specific-heat data with applied magnetic field for all the series are being collected and will be published elsewhere. In order to clarify these points, the microscopic magnetic structure of this family should be studied by magnetic x-ray or neutron diffraction.

To gain further insights about the CEF effects to the specific heat and the magnetic susceptibility, Fig. 2 and the inset of Fig. 3 present the experimental data when R = (a) Tb, (b) Dy, (c) Ho, and (d) Er together with the best fit to the data using our spin model (solid lines) described below. The best set of parameters is obtained from simultaneous minimization process of both $\chi(T)$, $\boldsymbol{M}(\boldsymbol{H})$ and C_{mag}/T data. A reasonable agreement between the experimental data and the fitting is also obtained for the heat capacity data except around $T \approx T_N$ where the contribution of magnetic fluctuations is important. In particular, for these compounds, it is observed that these fluctuations persist in a broad temperature range at the vicinity of T_N. This is reflected in the comparison between the experimental data and calculated curves, where

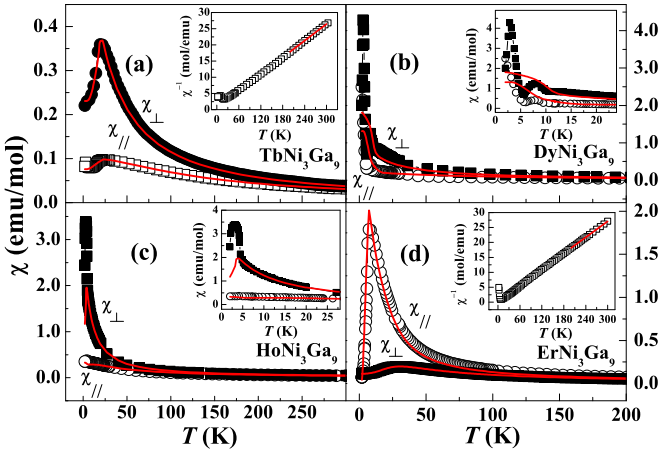

FIG. 2. Temperature dependence of the magnetic susceptibility for (a) $TbNi_3Ga_9$, (b) $DyNi_3Ga_9$, (c) $HoNi_3Ga_9$, and (d) $ErNi_3Ga_9$ measured for magnetic field of $H = 1$ kOe applied parallel $\chi_{//}$ (open symbols) and perpendicular $\chi_\perp$ (filled symbols) to the trigonal c axis. The solid lines are best fits to the data for both directions using our mean-field model (see below). The insets in (a) and (d) represent the inverse $1/\chi_{poly}(T)$ of polycrystalline susceptibility fitted with a linear Curie-Weiss law for $T > 100$ K. From this fitting we extracted the μ_{eff} and Θ_{CW} magnitudes for all compounds (see Table I). The insets in (b) and (c) show the low-T region and the presence of more complex ground states.

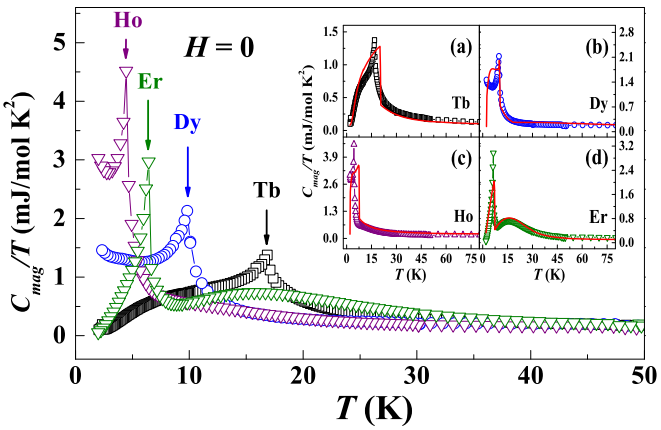

FIG. 3. Main panel: Magnetic contribution to the specific heat divided by temperature for $TbNi_3Ga_9$, $DyNi_3Ga_9$, $HoNi_3Ga_9$, and $ErNi_3Ga_9$. The inset shows the C_{mag}/T data for Tb-, Dy-, Ho-, and Er-based samples together with the best fit to the data of the mean-field model [11,12].

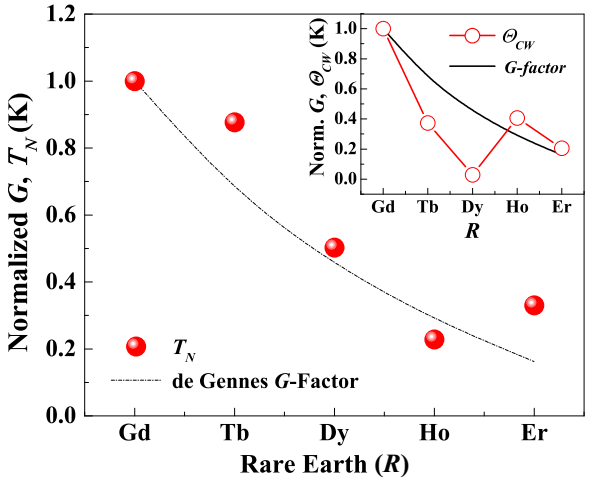

FIG. 4. Evolution of the normalized Neel temperature (T_N) for RNi$_3$Ga$_9$ (R = Tb, Dy, Ho, and Er) and de Gennes factors $G = (g_J - 1)^2 J(J+1)$ for R atoms (R = Tb, Dy, Ho, and Er). The inset shows the evolution of the normalized Θ_{CW} together with G.

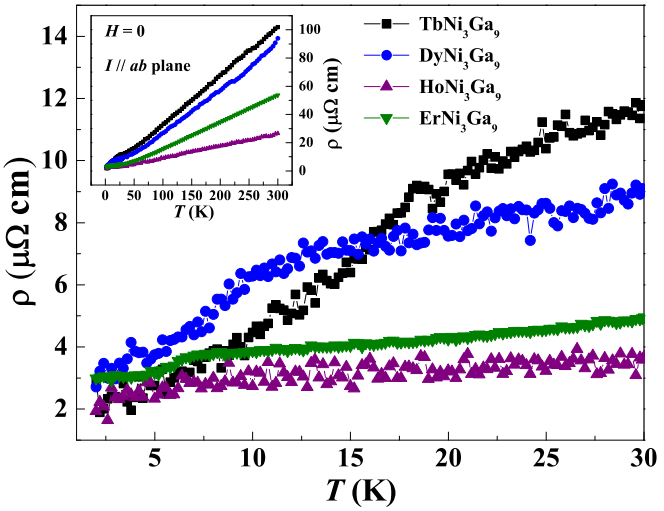

FIG. 5. Temperature dependence of the electrical resistivity for the RNi$_3$Ga$_9$ single crystal in the low-T region showing the change in slope at T_N. The current (I) has been applied parallel to the ab plane. The inset shows the full temperature range.

the temperatures at which the anomalies appear do not coincide with the observed maxima but with the inflection points in the experimental data.

Figure 4 presents the evolution of the T_N and Curie-Weiss temperature Θ_{CW} (inset) for the rare-earth-based compounds studied in this paper. They both have been compared to the de Gennes factor $G = (g_J - 1)^2 J(J+1)$ (dashed curves) for the ground-state multiplet J of each rare earth. The data are normalized by the T_N and Θ_{CW} values of the GdNi$_3$Ga$_9$ compound, as well as with the G value for the Gd ion. The Gd-based compound was also synthesized but the complete characterization of its physical properties data will be presented elsewhere along with experiments of electron-spin resonance. The data in Fig. 4 suggest that the long-range antiferromagnetic temperature and Curie-Weiss temperature, Θ_{CW}, do not rigorously follow the G scale. This behavior signals the presence of relevant CEF effects in determining the magnetic properties along the series, which are not included into the G factor [14–16]. Furthermore, considering the complex magnetic behavior at low T for R = Dy and Ho compounds (e.g., the metamagnetic transitions at $T = 2$ K), we must expect a deviation of T_N and Θ_{CW} from a simple de Gennes scale for these compounds.

The temperature dependence of the electrical resistivity, at $H = 0$ and applied current along the ab plane, for the RNi$_3$Ga$_9$ single crystals is plotted in Fig. 5. At high temperature, the data always showed a metallic behavior while, at low temperatures, a clear kink can be seen at the onset of the AFM order (T_N) for all studied compounds. The observed temperature values at the change in slope coincide well with the T_N values observed in the susceptibility and specific-heat data.

The magnetization data at $T = 2$ K for RNi$_3$Ga$_9$ (R = Tb to Er) for the magnetic field applied along the trigonal c axis ($H//c$) and in the basal plane ($H \perp c$) are shown in Fig. 6. Closed and open symbols have been used to identify the $H \perp c$ and $H//c$ data, respectively. Despite the anomalies observed below T_N at $H = 1$ kOe (Fig. 2), our $M(H)$ data also indicate that the axis of easy magnetization is perpendicular to the c axis for R = Tb, Dy, and Ho, whereas for R = Er it is parallel to the c axis. In the M versus H curves, for R = Tb [Fig. 6(a)] no metamagnetic transitions are observed up to 70 kOe and the magnetization increases almost linearly with H along both directions. The saturation Tb moment (9.72 μ_B) has not been attained up to the highest applied field. For R = Dy [Fig. 6(b)], multiple transitions are observed with H along the ab plane, suggesting that spin reorientations are taking place with applied field. A change in $M(H)$ between 40 and 60 kOe can be also observed for $H//c$.

This behavior may be associated with additional magnetic transitions within the AFM state (e.g., spin reorientation) and

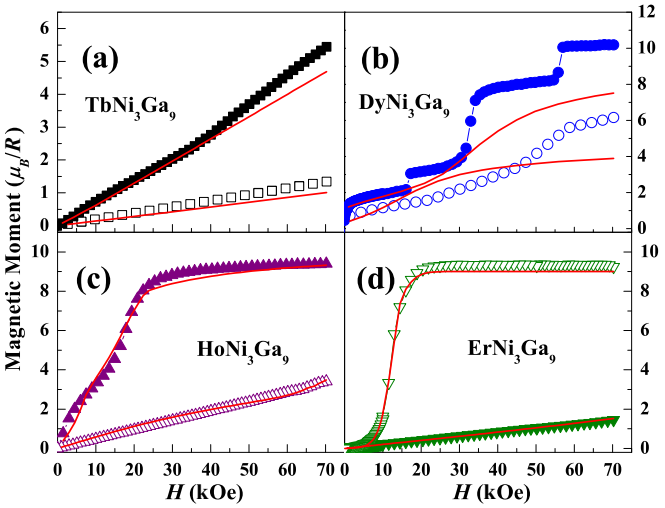

FIG. 6. Magnetization for (a) TbNi$_3$Ga$_9$, (b) DyNi$_3$Ga$_9$, (c) HoNi$_3$Ga$_9$, and (d) ErNi$_3$Ga$_9$ under applied magnetic perpendicular (filled symbols) and field parallel (empty symbols) to the c axis. All datasets were collected at $T = 2$ K. The solid lines represent the results from the spin model fittings.

TABLE II. Parameters extracted from the best fits to the spin model. All values are in Kelvin.

	B_0^2	B_0^4	B_3^4	B_0^6	B_3^6	B_6^6	z_1K_1	z_2K_2	z_1j_1	z_2j_2
$TbNi_3Ga_9$	1.10	0.10×10^{-04}	−0.24	0.10×10^{-03}	0.15×10^{-02}	-0.64×10^{-04}	2.3×10^{-03}	2.2×10^{-03}	0.57	−0.14
$DyNi_3Ga_9$	0.77	0.36×10^{-03}	0.23×10^{-01}	0.19×10^{-04}	0.13×10^{-03}	-0.73×10^{-03}	1.4×10^{-02}	0.0	0.23	−0.014
$HoNi_3Ga_9$	0.36	-0.15×10^{-02}	0.00	-0.13×10^{-04}	0.00	-0.85×10^{-04}	0.0	0.0	0.075	−0.002
$ErNi_3Ga_9$	−0.35	0.20×10^{-03}	0.86×10^{-02}	-0.42×10^{-05}	-0.40×10^{-04}	0.42×10^{-06}	-5.2×10^{-03}	3.6×10^{-03}	0.07	-1.0×10^{-04}

agrees with the one observed in the susceptibility data (see Fig. 2) of this compound for $H = 1$ kOe (along both directions) and with the increase in the specific-heat data below T_N at $H = 0$ (see Fig. 3). For R = Ho [Fig. 6(c)], the saturation is attained already at about $H = 30$ kOe after a metamagnetic transition is observed for $H \perp c$ between 10 and 20 kOe. Finally, for $ErNi_3Ga_9$ a transition takes place along the c axis for applied field of about H = 10–15 kOe up to the saturation, where the magnetic moment of ∼9.6 μ_B/Er^{3+} is recovered. No transition is observed for the field along the ab plane. The results in Fig. 6 are an indication that microscopic measurements, such as neutron and/or magnetic x-ray diffraction and NMR, as well as macroscopic field dependent susceptibility and specific-heat data, would be valuable in determining the magnetic structure evolution and clarify the ground state in these compounds. Considering the anisotropy observed for all cases, the magnetocrystalline anisotropy should be an important energy scale in this family.

As it has been shown, the magnetic structure of the series of intermetallics compounds $Tb_mRh_nIn_{3m+2n}$ (m = 1, 2; n = 0, 1) [17], $CeCd_{0.7}Sb_2$ [18], RRh_4B_4 [19], $RRhIn_5$ [20], and RNi_3Al_9 (R = Gd to Lu) [8] is related to the evolution of the sign of the CEF parameter B_0^2. In order to check for the above results, we present below the spin model used to simulate the magnetic properties of the system under study.

A. Evolution of CEF with *R*

To determine microscopic interactions and CEF parameters, magnetization and specific heat have been computed using a spin model. The model includes anisotropic first-neighbor RKKY interaction, a quadropolar first-neighbor coupling, and the CEF Hamiltonian corresponding to C_{3v} point symmetry [21]. Specifically we use the Hamiltonian

$$H = H_{\rm CEF} + \sum_{i,k} j_{i,k}\vec{J}_i\cdot\vec{J}_k + \sum_{i,k} K_{i,k}O_2^0(i)O_2^0(k) - g\mu_B\vec{H}_0\cdot\sum_i \vec{J}_i \quad (1)$$

The second term to the right is the superexchange (RKKY) interaction between the J_i and J_k moments. Following Ref. [22] we include in the third term a magnetic quadrupolar interaction between the J_i and J_k magnetic moments [$O_2^0 = 3J_z^2 - J(J+1)$]. This interaction can have its origin on magnetoelastic couplings or, more probably, like the RKKY interaction, via the propagation of conduction electrons [22]. The fourth term represents the Zeeman effect with an applied field $\vec{H}_0$. The first term is the CEF Hamiltonian and it is defined as [23]

$$H_{\rm CEF} = \sum_i H_{\rm CEF}(i) = \sum_{i,n,m} B_n^m(i)O_n^m(i) \quad (2)$$

where O_m^n are the Stevens equivalent operators (they describe the CEF in terms of powers of the local moments J). B_n^m characterize the crystal-field parameters for C_{3v} point symmetry and are experimentally determined. The list of CEF parameters is shown in Table II. Additionally, it is worth commenting that we have adopted the crystallographic c direction as the z-quantization axis.

The Hamiltonian given by Eq. (1) is solved within the mean-field approximation [24]. As the distance of R between planes (∼9 Å) is much larger than the in-plane distance (∼4 Å for first and ∼7 Å for second neighbors) we neglect the interplane coupling [25]. The hexagonal R plane is divided on two sublattices of sites A and B. In this approximation the antiferromagnetic coupling is limited to j_1, which couples spins on both A and B subnetworks while j_2 couples spins on the same sublattices. We have considered quadrupolar couplings K_1 (K_2) between magnetic moments on different (same) sublattices (see Fig. 7). Finally the mean-field Hamiltonian is simply

$$H_{\rm MF} = \sum_{i\in A} H_A + \sum_{i\in B} H_B, \quad (3)$$

$$\begin{aligned} H_X = {} & 2z_1j_1\vec{J}_X\cdot\langle\vec{J}_{\bar{X}}\rangle - z_1j_1\langle\vec{J}_A\rangle\cdot\langle\vec{J}_B\rangle + 2z_2j_2\vec{J}_X\cdot\langle\vec{J}_X\rangle \\ & - z_2j_2\langle\vec{J}_X\rangle\cdot\langle\vec{J}_X\rangle + 2z_1K_1O_2^0(X)\langle O_2^0(\bar{X})\rangle \\ & - z_1K_1\langle O_2^0(A)\rangle\langle O_2^0(B)\rangle + 2z_2K_2O_2^0(X)\langle O_2^0(X)\rangle \\ & - z_2K_2\langle O_2^0(X)\rangle\langle O_2^0(X)\rangle + H_{\rm CEF}(X) - g\mu_BH_0\cdot\vec{J}_X \end{aligned} \quad (4)$$

where the usual mean-field decoupling of the interaction

$$J_X\cdot J_{X'} \sim J_X\cdot\langle J_{X'}\rangle + \langle J_X\rangle\cdot J_{X'} - \langle J_X\rangle\cdot\langle J_{X'}\rangle \quad (5)$$

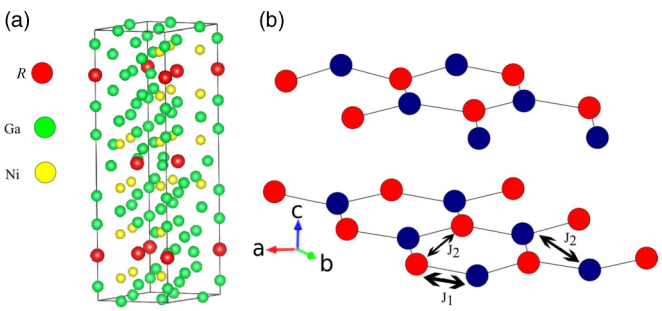

FIG. 7. (a) Crystal structure of RNi_3Ga_9 (R = rare earth). (b) Planes of R. Sublattices A and B are shown in red and blue. J_1 and J_2 are magnetic exchange interactions. Quadrupolar couplings K_1 and K_2 act on the same links as J_1 and J_2.

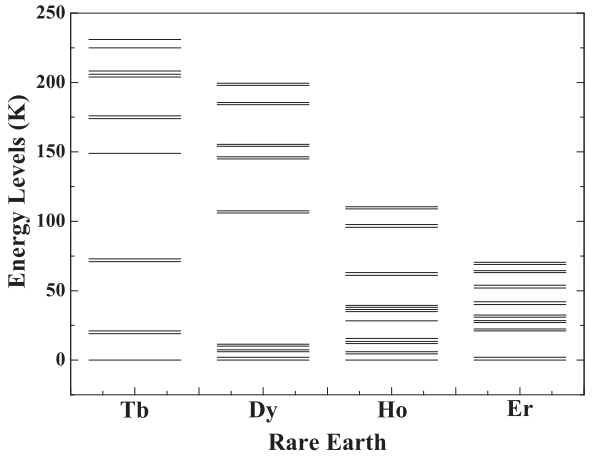

FIG. 8. CEF splitting of the ground-state multiplet obtained from the simulations of Figs. 2, 3, and 6 for $TbNi_3Ga_9$, $DyNi_3Ga_9$, $HoNi_3Ga_9$, and $ErNi_3Ga_9$.

(and a similar approximation for the quadrupolar term) has also been done. The mean value of the operators J_i ($O^0_{2,i}$) has been replaced by a sub-lattice-dependent mean value $\langle J_i\rangle = \langle J_X\rangle$ ($\langle O^0_{2,i}\rangle = \langle O^0_{2,X}\rangle$), where $X = A(B)$ if $i \in A(i \in B)$. $\bar{X}$ denotes the opposite sublattice ($\bar{A} = B, \bar{B} = A$). $z_1 = 3$ ($z_2 = 6$) is the number of first (second) neighbors. $H_{\rm MF}$ is solved self-consistently for each temperature and magnetic field. Magnetic couplings and CEF parameters come from the simultaneous fit to the magnetic experimental data (susceptibility, specific heat, and magnetization).

The best fits to our macroscopic data yield the parameters presented in Table II. The CEF level scheme obtained from the splitting of the R^{3+} J's multiplet, given by the above parameters, is shown in Fig. 8. Energy levels and wave functions are presented in Table III. The degeneracy of these states agrees with the one expected for a hexagonal symmetry [21] .

At this level of approximation the quadrupolar terms act as an effective additional crystal-field term $\Delta B^0_2 = 2z_i K_i \langle O^0_2\rangle$,$i = 1,2$ [see Eq. (4)] of second order that depends on temperature and magnetic field (because $\langle O^0_2\rangle$ depends on those parameters). For all R, except for Ho, which has $K_i = 0$, the quadrupolar interaction is such that it trays to align the magnetic moments with the z axis. In the case of Er, the magnetic moments align parallel to the z axis, so $\langle O^0_2\rangle > 0$ and, given that $z_1K_1 < 0$, $\Delta B^0_2(\text{Er}) < 0$ and the quadrupolar interaction reinforces the crystal-field effect. For Tb the spin lays in the plane and given that $z_1K_1 = 2.3$ mK > 0 it also gives $\Delta B^0_2(\text{Tb}) < 0$. We can estimate its maximum contribution taking $\langle O^0_2\rangle = -J(J+1) = -42$ and estimate the maximum value of $\Delta B^0_2(\text{Tb}) \sim -0.1$ K, which is smaller than $B^0_2 = 1.09$ K (a similar small contribution comes from K_2). For Dy, $K_1 = 14$ mK and the lowest value of O^0_2 (at $T = 0$) is

$$\langle O^0_2\rangle = 3 \times \frac{1}{2}^2 - \frac{15}{2}\left(\frac{15}{2}+1\right) = -\frac{252}{4} = -63$$

so $\Delta B^0_2(\text{Dy}) \sim K_1\langle O^0_2\rangle = 0.014$ K $\times (-63) = -0.88$ K. For this ion the quadrupolar interaction could modify the sign of $B^0_2 = 0.72$ K. But the actual maximum value of $\langle O^0_2\rangle$ in our calculation is ~ -34, which is not enough to modify the sign of B^0_2. In all situations this anisotropic contribution is smaller than the CEF contribution that comes from B^0_2 and does not modify the spin orientation. Nevertheless it is fundamental to obtain a simultaneous good fit to all the magnetic data.

The zero value of K_1 found for Ho can be explained if we notice that the CEF parameters B^m_n in Eq. (2) are related to the actual lattice CEF parameters A^m_n [26], which are approximately independent of the R. In particular $B^0_2 = \langle r^2\rangle\theta_2 A^0_2$, where $\langle r^2\rangle$ is the average of r^2 over the $4f$ shell and θ_2 is a geometrical factor (θ_2 is the second-order Stevens factor for the R). θ_2 is tabulated in Ref. [26] and the values for $\langle r^2\rangle$ were computed in Ref. [27] for free R ions. In general, the $\langle r^n\rangle$ values depend on the host, whether it is an insulating [28] or a metallic [29] environment. But for the same environment the variations are small for different R. If the different R do not distort the electron density in their neighborhood, the net perturbation should be comparable for both ions. Therefore, the ratio $\frac{B^0_2}{\theta_2}$ should not depend much on the R ion itself. In fact that is seen with the values reported in Table I ($\frac{B^0_2}{\theta_2} \sim 140 \pm 20$ for all R). We can use this to infer from $\Delta B^0_2(\text{Tb})$ the value of z_1K_1 for Ho: $\frac{\Delta B^0_2(\text{Tb})}{\theta_2(\text{Tb})} \sim \frac{\Delta B^0_2(\text{Ho})}{\theta_2(\text{Ho})} = \frac{2z_1K_1(\text{Ho})\langle O^0_2\rangle(\text{Ho})}{\theta_2(\text{Ho})}$. As Ho magnetic moments order in plane as Tb, $\langle O^0_2\rangle(\text{Ho}) = -J \times (J+1) = -72$ and $z_1K_1(\text{Ho}) = \frac{\Delta B^0_2(\text{Tb})}{\langle O^0_2\rangle(\text{Ho})}\frac{\theta_2(\text{Ho})}{\theta_2(\text{Tb})} \sim 0.3$ mK. This result is an order of magnitude smaller than the values obtained for the other Rs and could be too small to be captured by our fits.

It is worth commenting that the obtained B^2_0 and exchange constants account for the main features of the data shown in Figs. 2–4 and 6, meaning that the evolution of the magnetic properties of these compounds along the series is all well explained by this model. However, it is important to notice that the CEF parameters obtained from the fits to macroscopic measurements data may not be as precise and unique and additional experiments for the direct determination of the CEF scheme by inelastic neutron scattering and/or x-ray absorption for these compounds are highly desirable. Nevertheless, qualitative trends in the evolution of the CEF effects and exchange constants that play a role in the magnetic properties of the studied series are totally captured by our model. As such, the evaluation of B^2_0 along the studied compounds is consistent with the change in easy axis magnetization from *ab* plane to *c* axis (see Fig. 2), that is, the B^2_0 parameter is positive for R = Tb, Dy, and Ho and negative for R = Er. Additionally, the existence of competing and antiferromagnetic and ferromagnetic exchange constants—the j_1 and j_2 parameter, respectively—explains the complex low-T magnetic behavior of these compounds that can present spin-flop or metamagnetic transitions and/or changes in the magnetic structure in the ordered state, especially when the field is applied along the easy axis. In fact, a change in sign of the CEF parameters B^2_0 has been observed along a series of R-based low-symmetry layered compounds as the lattice-parameter ratio *c/a* changes [18]. Consistent with the previous finding, the *c/a* ratio in this series of compounds increases from *c/a* ~3.7854 for the Tb compound to 3.7872 for the Er counterpart.

TABLE III. Kramers doublet eigenvalues (E_i) and associated eigenfunctions (ϕ_i) for Ho^{3+} ($J = 8$), Er^{3+}, Dy^{3+} ($J = 15/2$), and Tb^{3+} ($J = 6$) ions in RNi_3Ga_9.

Ion	E_i(K)	ϕ_i
Tb^{3+}	0.0	$0.026\|-6\rangle - 0.375\|-3\rangle + 0.847\|0\rangle + 0.375\|3\rangle + 0.026\|6\rangle$
	21.0	$\mp0.160\|\mp5\rangle + 0.292\|\mp2\rangle + \mp0.804\|\pm1\rangle - 0.493\|\pm4\rangle$
	74.5	$\pm0.250\|\mp4\rangle - 0.220\|\mp1\rangle + \pm0.661\|\pm2\rangle + 0.672\|\pm5\rangle$
	149.7	$0.129\|-6\rangle - 0.695\|-3\rangle - 0.695\|3\rangle - 0.129\|6\rangle$
	176.6	$-0.372\|\mp4\rangle + \mp0.144\|\mp1\rangle - 0.607\|\pm2\rangle + \pm0.688\|\pm5\rangle$
	206.2	$0.223\|\mp5\rangle + \pm0.331\|\mp2\rangle + 0.534\|\pm1\rangle + \mp0.746\|\pm4\rangle$
	208.4	$-0.417\|-6\rangle + 0.476\|-3\rangle + 0.446\|0\rangle - 0.476\|3\rangle - 0.417\|6\rangle$
	225.7	$0.695\|-6\rangle + 0.129\|-3\rangle + 0.129\|3\rangle - 0.695\|6\rangle$
	231.6	$0.570\|-6\rangle + 0.365\|-3\rangle + 0.288\|0\rangle - 0.365\|3\rangle + 0.570\|6\rangle$
Dy^{3+}	0.0	$-0.31\|\mp13/2\rangle + \mp0.06\|\mp7/2\rangle - 0.82\|\mp1/2\rangle + \pm0.03\|\pm5/2\rangle - 0.47\|\pm11/2\rangle$
	6.9	$\pm0.06\|\mp15/2\rangle - 0.15\|\mp9/2\rangle + \pm0.74\|\mp3/2\rangle - 0.31\|\pm3/2\rangle + \pm0.57\|\pm9/2\rangle - 0.10\|\pm15/2\rangle$
	10.0	$-0.12\|\mp11/2\rangle + \mp0.73\|\mp5/2\rangle - 0.01\|\pm1/2\rangle + \mp0.66\|\pm7/2\rangle + 0.14\|\pm13/2\rangle$
	106.9	$0.53\|\mp11/2\rangle + \mp0.21\|\mp5/2\rangle + 0.01\|\pm1/2\rangle + \mp0.05\|\pm7/2\rangle - 0.82\|\pm13/2\rangle$
	145.0	$-0.39\|\mp13/2\rangle + \mp0.27\|\mp7/2\rangle + 0.55\|\mp1/2\rangle + \pm0.21\|\pm5/2\rangle - 0.66\|\pm11/2\rangle$
	154.1	$-0.18\|\mp15/2\rangle + \pm0.19\|\mp9/2\rangle - 0.53\|\mp3/2\rangle + \mp0.01\|\pm3/2\rangle + 0.68\| \pm 9/2\rangle + \mp0.43\|\pm15/2\rangle$
	184.2	$0.21\|\mp11/2\rangle + \mp0.62\|\mp5/2\rangle - 0.14\|\pm1/2\rangle + \pm0.70\|\pm7/2\rangle + 0.25\|\pm13/2\rangle$
	198.3	$\pm0.03\|\mp15/2\rangle + 0.17\|\mp9/2\rangle + \mp0.20\|\mp3/2\rangle - 0.19\|\pm3/2\rangle + \pm0.35\|\pm9/2\rangle + 0.88\|\pm15/2\rangle$
Ho^{3+}	0.0	$0.707\|-3\rangle + 0.707\|3\rangle$
	4.5	$0.49\|\mp4\rangle + 0.87\|\pm2\rangle + 0.07\|\pm8\rangle$
	12.3	$0.24\|\mp5\rangle + 0.97\|\pm1\rangle + 0.06\|\pm7\rangle$
	15.6	$0.11\|-6\rangle + 0.99\|0\rangle + 0.11\|6\rangle$
	28.2	$0.707\|-3\rangle + 0.707\|3\rangle$
	35.2	$0.73\|\mp4\rangle + \mp0.36\|\pm2\rangle + \mp0.58\|\pm8\rangle$
	38.0	$0.48\|\mp4\rangle + \mp0.34\|\pm2\rangle + 0.81\|\pm8\rangle$
	61.6	$0.03\|\mp7\rangle + 0.24\|\mp1\rangle + 0.97\|\pm5\rangle$
	95.6	$0.707\|-6\rangle + 0.707\|6\rangle$
	97.6	$0.70\|-6\rangle + 0.15\|0\rangle + 0.70\|6\rangle$
	109.7	$0.01\|\mp5\rangle + 0.06\|\pm1\rangle + 0.998\|\pm7\rangle$
Er^{3+}	0.0	$\|\pm15/2\rangle$
	20.8	$\mp0.02\|\pm1/2\rangle + 0.13\|\pm7/2\rangle + \mp0.99\|\pm13/2\rangle$
	26.8	$\pm0.02\|\mp1/2\rangle - 0.22\|\pm5/2\rangle + \pm0.98\|\pm11/2\rangle$
	31.6	$\mp0.23\|\pm3/2\rangle + 0.97\|\pm9/2\rangle$
	40.2	$-0.03\|\mp11/2\rangle + \pm0.07\|\mp5/2\rangle + 0.24\|\pm1/2\rangle + \mp0.96\|\pm7/2\rangle - 0.13\|\pm13/2\rangle$
	52.2	$\pm0.01\|\mp13/2\rangle - 0.12\|\mp7/2\rangle + \pm0.19\|\mp1/2\rangle - 0.95\|\pm5/2\rangle + \mp0.22\|\pm11/2\rangle$
	62.9	$\mp0.97\|\pm3/2\rangle - 0.23\|\pm9/2\rangle$
	69.3	$0.03\|\mp11/2\rangle + \mp0.21\|\mp5/2\rangle + 0.95\|\pm1/2\rangle + \pm0.22\|\pm7/2\rangle + 0.01\|\pm13/2\rangle$

IV. CONCLUSIONS

In this paper, we have synthesized the family of intermetallic compounds RNi_3Ga_9 (R = Tb, Dy, Ho, and Er) in single-crystal form. Magnetization as a function of temperature and magnetic field, electrical resistivity, and heat-capacity measurements have been used to explore their physical properties. A strong magnetic anisotropy observed in magnetic susceptibility curves was attributed to CEF effects. Based on this fact, we were able to fit the observed temperature dependence of the specific heat and the anisotropic features in the magnetic susceptibility using a spin model that includes the CEF effects and competing antiferromagnetic and ferromagnetic exchange constants. From these data, a CEF level scheme was obtained for each rare earth. Interestingly, the behavior observed in T dependence of the magnetic susceptibility, where the antiferromagnetic easy axis is along the ab plane for the compounds with R = Tb, Dy, and Ho, while it is along the c axis for the compound with R = Er, was found to be correlated to the sign of CEF parameter B_0^2. The sign of this parameter can change as a result of the evolution of the structural lattice parameters along the series.

ACKNOWLEDGMENTS

The authors thank Brazilian agencies Conselho Nacional de Desenvolvimento Científico e Tecnológico (CNPq) (Grants No. 442230/2014-1, No. 3046449/2013-9, No. 309647/2012-6, No. 304649/2013-9, No. 157835/2015-4, and No. 455970/2014-9), Fundação de Amparo a Pesquisa do Estado de São Paulo (FAPESP) (Grant No. 2012/04870-7),

Fundação de Amparo a Pesquisa do Estado de Minas Gerais (FAPEMIG-MG) (Grant No. APQ-02256-12) and Coordenação de Aperfeiçoamento de Pessoal de Nível Superior (CAPES) for financial support.

[1] S. Qimiao and F. Steglich, Science **329**, 1161 (2010).
[2] S. Ohara, T. Yamashita, Y. Mori, and I. Sakamoto, J. Phys. Conf. Ser. **273**, 012048 (2011).
[3] T. Yamashita, R. Miyazaki, Y. Aoki, and S. Ohara, J. Phys. Soc. Jpn. **81**, 034705 (2012).
[4] Y. Utsumi *et al.*, Phys. Rev. B **86**, 115114 (2012).
[5] K. Matsubayashi, T. Hirayama, T. Yamashita, S. Ohara, N. Kawamura, M. Mizumaki, N. Ishimatsu, S. Watanabe, K. Kitagawa, and Y. Uwatoko, Phys. Rev. Lett. **114**, 086401 (2015).
[6] R. E. Gladyshevskii, K. Cenzual, H. D. Flack, and E. Parthé, Acta Cryst. **B49**, 468 (1993).
[7] Y. Lutsyshyn, Y. Tokaychuk, V. Davydov, and R. Gladyshevskii, Chem. Met. Alloys **1**(3/4), 303 (2008).
[8] T. Yamashita, S. Ohara, and I. Sakamoto, J. Phys. Soc. Jpn. **80**, SA080 (2011).
[9] Z. Fisk and J. P. Remeika, in *Handbook on the Physics and Chemistry of Rare Earths*, edited by K. A. Gshneidner and L. Eyring (Elsevier, Amsterdam 1989), Vol. 12, Chap. 81, pp. 53–71.
[10] P. C. Canfield and Z. Fisk, Philos. Mag. B **65**, 1117 (1992).
[11] P. G. Pagliuso, D. J. Garcia, E. Miranda, E. Granado, R. Lora-Serrano, C. Giles, J. G. S. Duque, R. R. Urbano, C. Rettori, J. D. Thompson, M. F. Hundley, and J. L. Sarrao, J. Appl. Phys. **99**, 08P703 (2006).
[12] R. Lora-Serrano, C. Giles, E. Granado, D. J. Garcia, E. Miranda and O. Agüero, L. Mendonça Ferreira, J. G. S. Duque, and P. G. Pagliuso, Phys. Rev. B **74**, 214404 (2006).
[13] V. Petricek, M. Dusek, and L. Palatinus, Z. Kristallogr. **229**(5), 345 (2014).
[14] P. G. Pagliuso, J. D. Thompson, M. F. Hundley, J. L. Sarrao, and Z. Fisk, Phys. Rev. B **63**, 054426 (2001).
[15] C. B. R. Jesus, M. M. Piva, P. F. S. Rosa, C. Adriano, and P. G. Pagliuso, J. Appl. Phys. **115**, 17E115 (2014).
[16] C. B. R. Jesus, M. M. Piva, P. F. S. Rosa, C. Adriano, Z. Fisk, and P. G. Pagliuso, Phys. Procedia **75**, 618 (2015).
[17] R. Lora-Serrano, L. Mendonça Ferreira, D. J. Garcia, E. Miranda, C. Giles, J. G. S. Duque, E. Granado, and P. G. Pagliuso, Physica B **348**, 326 (2006).
[18] P. F. S. Rosa, R. J. Bourg, C. B. R. Jesus, P. G. Pagliuso, and Z. Fisk, Phys. Rev. B **92**, 134421 (2015).
[19] B. D. Dunlap, L. N. Hall, F. Behroozi, G. W. Crabtree, and D. G. Niarchos, Phys. Rev. B **29**, 6244 (1984).
[20] N. V. Hieu, T. Takeuchi, H. Shishido, C. Tonohiro, T. Yamada, H. Nakashima, K. Sugiyama, R. Settai, T. D. Matsuda, Y. Haga, M. Hagiwara, K. Kindo, S. Araki, Y. Nozue, and Y. Ōnuki, J. Phys. Soc. Jpn. **76**, 064702 (2007).
[21] U. Walter, J. Phys. Chem. Solids, **45** 401 (1984).
[22] J. Jensen and A. R. Mackintosh, *Rare Earth Magnetism: Structures and Excitations* (Clarendon, Oxford, 1991), Chap. 5.5; http://www.fys.ku.dk/∼jjensen/REM.htm, online version (2011).
[23] K. W. H. Stevens, Proc. Phys. Soc. London, Sect. A, **65** 209 (1952).
[24] See a nice description of the mean-field approximation on magnetic systems in Chap. 2.1 of Ref. [22].
[25] The interplane coupling is necessary to have long-range order at a nonzero temperature [30]. The lack of this coupling is compensated by the mean-field approximation that leads to a finite ordering temperature. In an effective form parameters $j_{1,2}$ and $K_{1,2}$ include the interplane coupling; Specific heat of quasi-two-dimensional antiferromagnetic Heisenberg models with varying interplanar couplings.
[26] M. T. Hutchings, in *Solid State Physics*, edited by F. Seitz and D. Turnbull (Academic, New York, 1964).
[27] A. J. Freeman and R. E. Watson, Phys. Rev. **127**, 2058 (1962).
[28] A. J. Freeman and J. P. Desclaux, J. Magn. Magn. Mater. **12**, 11 (1979).
[29] L. Steinbeck, M. Richter, H. Eschrig, and U. Nitzsche, Phys. Rev. B **49**, 16289 (1994).
[30] S. Blundell, *Magnetism in Condensed Matter* (Oxford University, United Kingdom, 2001), Chap. 6; P. Sengupta, A. W. Sandvik, and R. R. P. Singh, Phys. Rev. B **68**, 094423 (2003).